Ion Diffusivities in Nanoconfined Interfacial Water Films Contribute to Mineral Carbonation Thresholds

Journal:	*Environmental Science: Nano*
Manuscript ID	EN-ART-12-2019-001382.R1
Article Type:	Paper

Paper

Ion Diffusivities in Nanoconfined Interfacial Water Films Contribute to Mineral Carbonation Thresholds†

Received 00th January 20xx,
Accepted 00th January 20xx

DOI: 10.1039/x0xx00000x

Quin R.S. Miller[a,b]*, John P. Kaszuba[b,c], Sebastien N. Kerisit[a], H. Todd Schaef[a], Mark E. Bowden[d], B. Peter McGrail[e], and Kevin M. Rosso[a]

The dynamics and reactivity of nanoconfined fluids play critical roles across a wide range of environmental and technological systems, though reaction mechanisms and kinetics are not well understood. The carbonation kinetics of forsterite (Mg_2SiO_4) exposed to 90 atm supercritical carbon dioxide at 35-65 °C and 85-100% relative humididty (RH) was monitored with *in situ* X-ray diffraction, and partner molecular dynamics simulations were used to describe the free energy landscape of Mg^{2+} adsorption and diffusion on forsterite surfaces covered in water films 3-10 monolayers thick. The collective findings reveal how decreasing the water film thickness by ~1.4 monolayers, from ~0.92 to ~0.64 nm, inhibited reaction rates by up to 97%, promoted anhydrous Mg-carbonate (magnesite, $MgCO_3$) precipitation, and more than doubled the apparent activation energy of carbonation. The transport simulations suggest that four monolayers are required to enable sufficiently facile Mg^{2+} diffusion, helping explain previously observed water film thickness-dependent reactivity thresholds.

Environmental significance

Thin adsorbed water films are ubiquitous examples of nanoconfined environments, whose reactivity have broad implications for natural and engineered processes. This study uses coupled experiments and molecular modelling to determine Mg-silicate carbonation kinetics and energetics of Mg^{2+} diffusion as a function of water film thickness. Our results provide a better understanding of rates, mechanisms, and solute transport thresholds controlling physicochemical mineral transformations at complex interfaces in rocks, soil, and other porous media.

1. Introduction

Chemical transformations in nanoscale water films have poorly understood constraints and are difficult to directly probe, yet remain broadly relevant[1-8] across heterogeneous atmospheric chemistry[9], (extra)terrestrial soil-hosted reactions [10-13], energy storage [14, 15], water treatment[16], pharmaceutical stability[17], building materials[18, 19], hydrocarbon resource extraction[20-22], engineered barriers [23, 24], prebiotic chemistry[25, 26], and biomineralization[27, 28]. In the unique environment of thin water films, the local pH, metal and organic solubilities and speciation, and the effects of nanoconfinement are often major unknowns. The behavior of water as both a reactant and a solvent can diverge dramatically from bulk liquid due to the highly structured nature of nanoconfined H_2O.[29-31] In particular, the ordering and limited mobility of interfacial H_2O significantly lowers its dielectric constant[32-35] and diffusivity[29, 36-39] relative to bulk water, broadly impacting crystallization[40-44], lubrication[45, 46], electron transport[47-49], metal[4, 5, 50-52] and fluid sorption[4, 5, 50, 51, 53, 54], proton dynamics[55-57], H_2O dissociation[58, 59], crustal geodynamics[60], metal-organic complexation[61, 62], isotope exchange kinetics[63], carbonic acid generation[64], and ion hydration structure and energetics[65-67].

For example, in water-bearing (wet) supercritical CO_2 ($scCO_2$) at conditions relevant to CO_2 storage[68, 69] and enhanced hydrocarbon recovery[70], we recently demonstrated that the apparent activation energy (E_a) for magnesite ($MgCO_3$) precipitation between 50-90 °C in the ~<1 nm water films that condense onto forsterite (Mg_2SiO_4)[65] is greatly reduced. Related studies in this domain have likewise demonstrated unique mineral stabilities[71], precipitate morphologies[72], and solute transport properties[73]. A critical adsorbed water film thickness >65-70% relative humidity (RH) appears to be necessary for rapid and continuous carbonation of silicate minerals in wet $scCO_2$ at 50-160 °C and 89-178 atm.[74-76] At 50 °C and 89 atm, the experimentally-determined[74] reactivity threshold for forsterite carbonation corresponds to ~2.1-2.4 monolayers (ML) of adsorbed water.[63] Although this general phenomenon of water film thickness-dependent reactivity

---

[a] *Physical and Computational Sciences Directorate, Pacific Northwest National Laboratory, Richland, WA 99352, USA*
Email: quin.miller@pnnl.gov
[b] *Department of Geology and Geophysics, University of Wyoming, Laramie, WY 82071, USA*
[c] *School of Energy Resources, University of Wyoming, Laramie, WY 82071, USA*
[d] *Environmental Molecular Sciences Laboratory, Pacific Northwest National Laboratory, Richland, WA 99352, USA*
[e, 5] *Energy and Environment Directorate, Pacific Northwest National Laboratory, Richland, WA 99352, USA*

† Electronic Supplementary Information (ESI) available: Figure S1-S8 and Table S1-S2. Tabulated experimental parameters and results, *in situ* time-resolved XRD waterfall plots, supplementary XRD scans of reacted samples, and *ex situ* thermogravimetric-mass spectrometry measurements.
See DOI: 10.1039/x0xx00000x

thresholds in wet $scCO_2$ has been known for over a decade in the context of steel corrosion and rock carbonation[77, 78], the mechanistic origin of these unique reactivity thresholds and trends have remained unclear.

The goal of the present study was to help elucidate mechanisms, by quantitatively determining how mineral transformation kinetics vary as a function water film thickness and temperature. Our specific focus on the thin water film format is advantageous in that it minimizes possible geometric complications at the nanoscale such as three-dimensional steric hindrance[79], crystallization pressure[80], and wall curvature[81, 82]. It furthermore enables evaluation of one major hypothesis, that observed mineral reactivity thresholds are a direct consequence of solute mobility in the water film.

We used laboratory-based pressurized *in situ* powder X-ray diffraction (XRD)-derived kinetics to extend the range of conditions (temperature and water film thickness) probed by our recent forsterite carbonation study[65]. Synthetic forsterite nanoparticles were reacted in our *in situ* XRD cell with 100% or 85% water-saturated (relative humidity, RH) supercritical CO_2 at 90 atm, thereby varying the thickness of nanoscale adsorbed water films on forsterite particles. To help constrain mass transport kinetics, we employed molecular dynamics (MD) simulations[83] to estimate diffusion barriers of outer-sphere hydrated Mg^{2+} complexes in films 3-10 ML-thick, using forsterite (010) as the model surface. This combined approach revealed 1) a newly-delineated Mg-carbonate precipitation regime between 85-100% RH, and 2) a critical water film thickness of 4 ML to facilitate Mg^{2+} diffusion. The findings add new insights into controls on carbonation kinetics and the origin of reactivity thresholds in nanoconfined interfacial water films.

2. Materials and methods

2.1 Materials

Sodium chloride solutions were prepared with deionized distilled (DDI) water and Sigma Aldrich reagent-grade NaCl. High-surface area (26.7±0.1 m^2/g) synthetic forsterite[61, 62, 74, 84] was prepared using the procedure of Saberi et al.[85]. The forsterite, which has an average crystallite size of ~31 nm, matches the International Centre for Diffraction Data powder diffraction file (PDF) #34-0189. Other than trace (<2 wt %) periclase (MgO, PDF #45-0946) the material is virtually chemically pure, with <0.4 atomic percent sodium present. In addition to facilitating laboratory kinetics studies at hours-days timescales[61, 62, 65, 74], the high-surface area forsterite ensures that the water adsorption is not controlled by less hydrophilic secondary precipitates, and that steady-state[65, 74, 84] water film thicknesses may be reached. In contrast, carbonation of larger Ca-silicate particles (~10-100 μm) resulted in a 5X increase in specific surface area of the mineral assemblage, increasing the total amount of sorbed water and precluding water film thickness determination[75].

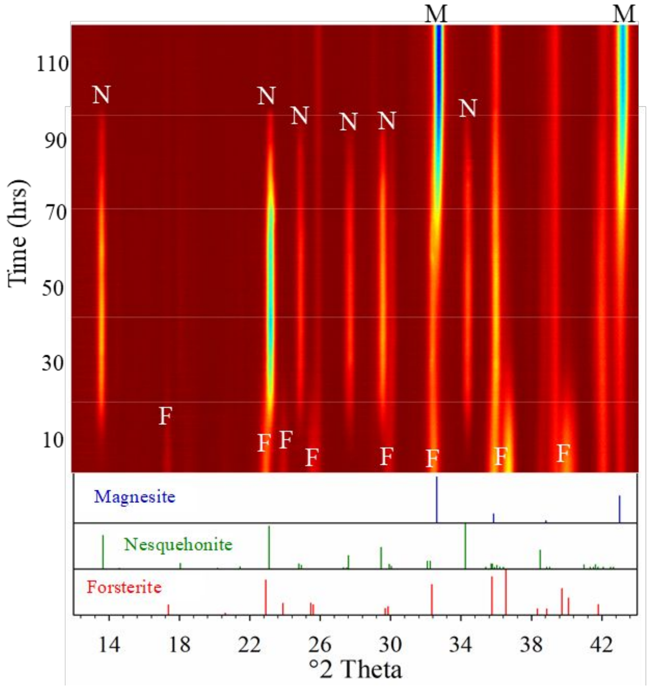

Fig. 1. Two-dimensional waterfall plot of **EXP 3** (50/100) time-resolved *in situ* diffractograms showing the dissolution of forsterite (F), precipitation of transient metastable nesquehonite (N), and precipitation of magnesite (M) at 50 °C and 90 atm $scCO_2$ at 100% RH. Three-dimensional plot shown in **Fig. S1**. The relative intensities are depicted with an inverse heat scale colour scheme and the powder diffraction (PDF) reference files are plotted for clarity. The PDF files for forsterite, nesquehonite, and magnesite are #34-0189, #20-0669, and #8-0479, respectively.

2.2 In situ X-ray diffraction

Time-resolved quantitative XRD experiments were conducted at 90 atm and 35-65 °C in a high-pressure static reactor with a beryllium cap and stainless-steel base. The *in situ* XRD experimental apparatus and procedures are described in detail elsewhere [61, 62, 75, 86, 87]. Briefly, the *in situ* XRD reactor was housed in a Bruker D8 Discover X-ray powder diffractometer equipped with a HI-STAR GADDS detector, an experimental configuration capable of analysing mineral assemblages at elevated pressure and temperature with a 45 kV and 200 mA Cu Kα-sourced microfocus X-ray beam. The diffractometer automatically scanned the sample for 200 seconds with a nine second delay in between each pattern.

The adsorbed water film thickness was controlled by imposing a relative humidity (RH) at 90 atm $scCO_2$ and 35-65 °C of either 100% or 85% RH. Experimental conditions are identified with a description that indicates the temperature and RH, while numbers identify individual experiments, as listed in **Table S1**. For example, the experiment conducted at 65 °C and 85% RH is **EXP 2** (65/85). An inexhaustible solution reservoir (10 μl) ensured constant RH of $scCO_2$ based on the equilibrium water concentrations of $scCO_2$ in contact with Mili-Q water or a concentrated NaCl solution[88]. The wet $scCO_2$ fluid induced the formation of adsorbed water films with steady-state thicknesses[63, 74, 84, 89]. which hosted CO_2 dissolution and $H_xCO_3^{(2-x)-}$ formation[63, 90], driving coupled forsterite dissolution and magnesite ($MgCO_3$) and/or nesquehonite ($MgCO_3 \cdot 3H_2O$)

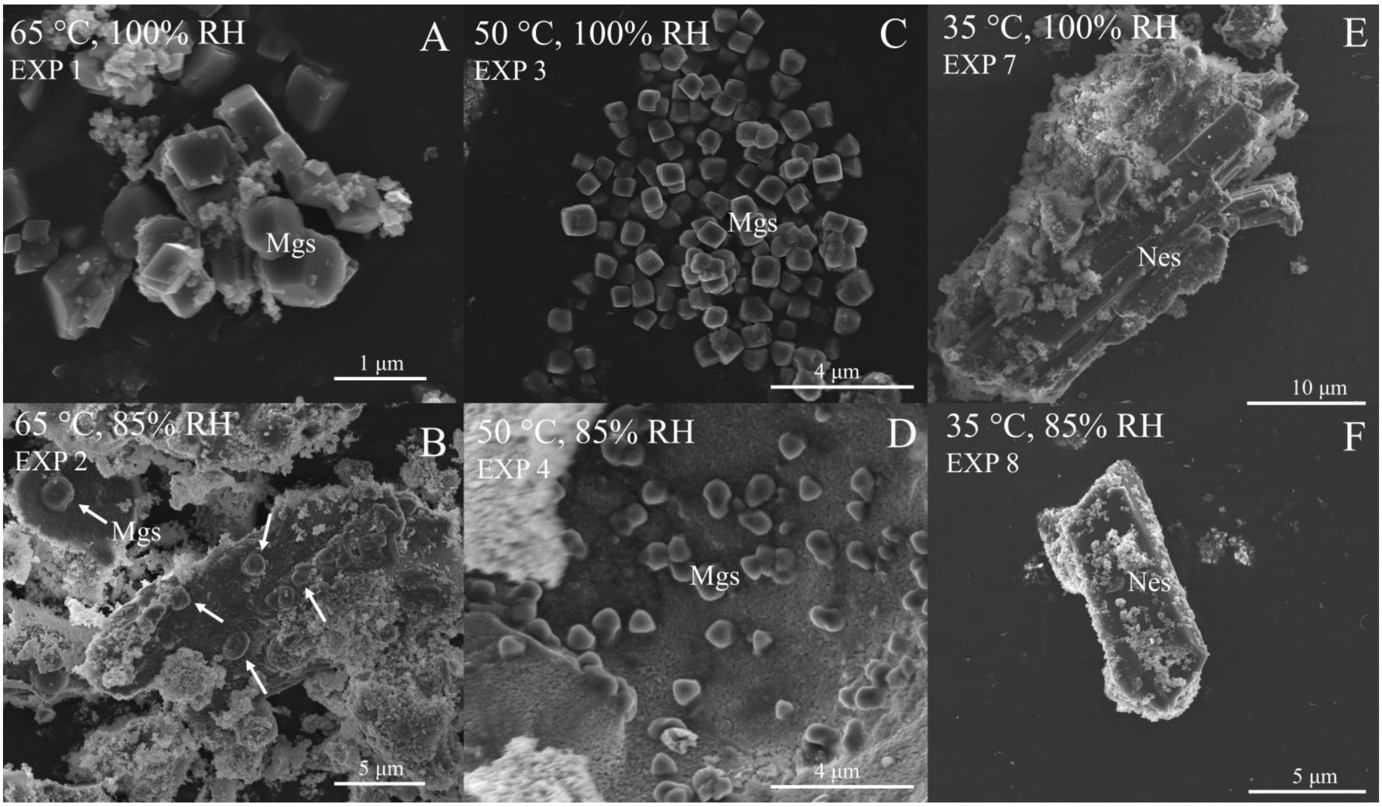

Fig. 2. Representative SEM photomicrographs of well-formed submicron magnesite (Mgs) rhombohedrals, bladed fragments of nesquehonite (Nes), and globular magnesite for samples reacted at 35-65 °C and 90 atm $scCO_2$ at 100% or 85% RH. (**Table S1**).

precipitation. Based on previous work on forsterite reactivity in H_2O-CO_2 fluids [61, 62, 65, 86, 91-94], the overall carbonation reactions are:

$$Mg_2SiO_4 + 2CO_2 = 2MgCO_3 + SiO_2(am)$$

(1)

and

$$Mg_2SiO_4 + 2CO_2 + 6H_2O = 2MgCO_3 \cdot 3H_2O + SiO_2(am) \quad (2)$$

Magnesite may also form from a metastable nesquehonite intermediate via the reaction:

$$MgCO_3 \cdot 3H_2O = MgCO_3 + 3H_2O \quad (3)$$

To date, investigations of mineral reactivity in water-bearing $scCO_2$[68] used deionized/distilled water, and varied water concentration in the $scCO_2$ by changing the mass of water in the reactor. Undersaturated conditions (e.g. 85% RH) could only be attained by placing less water than was needed to reach saturation for a given pressure and temperature, leaving open the possibility of systematic error associated with decreasing RH and thinner water films as water partitioned onto cold reactor components and/or was incorporated into hydrated precipitates during an experiment. Our approach eliminates experimental uncertainties inherent to measuring and dispensing ~1 µl-scale quantities of water and determining internal volumes of reactors.

Quantitative analysis of time-resolved diffraction patterns (e.g. **Fig. 1**) allowed the *in situ* crystalline phase abundances of the carbonating forsterite sample to be determined throughout the course of the experiments. The duration of the experiments ranged from 44.7-262.4 hours, which resulted in ~775 (**EXP 2**, 65/85) to >4000 (**EXP 7**, 35/100) discrete quantitative *in situ* XRD diffractograms (**Fig. S1**). This high temporal resolution enabled us to accurately determine reaction kinetics. Inconsequential gaps in the data collection for **EXP 2** and **EXP 7-8** were due to temporary computer outages that did not perturb the *in situ* XRD reactor temperature and pressure. Previously described[61, 62, 65] quantitative XRD analysis was carried out using full-pattern fitting with TOPAS software to obtain relative abundance (wt %) of each crystalline phase. Initial kinetic results for **EXP 1** (65/100) were previously reported based on the analysis of 24 time-resolved diffractograms[65], and the **EXP 1** results presented in this work are based on all 776 processed patterns. Patterns calculated from published crystal structures[95, 96 97] were matched to the experimental patterns using pseudo-Voigt line profiles and nesquehonite preferred orientation was modelled with a spherical harmonics approach [98].

2.3 Ex situ characterization of reacted samples

Reacted samples were characterized *ex situ* using the procedures of Miller et al. [62]. Briefly, thermogravimetric mass spectrometry (TGA-MS) was used to determine the extent of carbonation and distinguish between hydrous and anhydrous Mg-carbonates[62, 75, 87]. Scanning electron microscopy and energy dispersive spectroscopy (SEM-EDS) was used to determine the morphology and chemistry, respectively, of the Mg-carbonates. Reacted grains were mounted with adhesive carbon tape and coated with a 10-15 nm layer of carbon. Samples were imaged and analyzed with a FEI Helios NanoLab 600i microscope equipped with OXFORD Instruments INCA Energy Dispersive Spectroscopy X-ray detector calibrated with Cu foil.

Additionally, subsamples from **EXP 5** and **EXP 8** were analyzed with *ex situ* XRD to search for magnesite reflections at ~53.9 °2ϑ. The °2ϑ range of *in situ* XRD does not reach that value due to intense reflections at ~45 °2ϑ from the reactor's beryllium cap. Reacted subsamples were kept in the sample holder or placed in 0.6 mm Charles Supper Company borosilicate capillary tubes and patterns were collected with the detector at 40 °2ϑ.

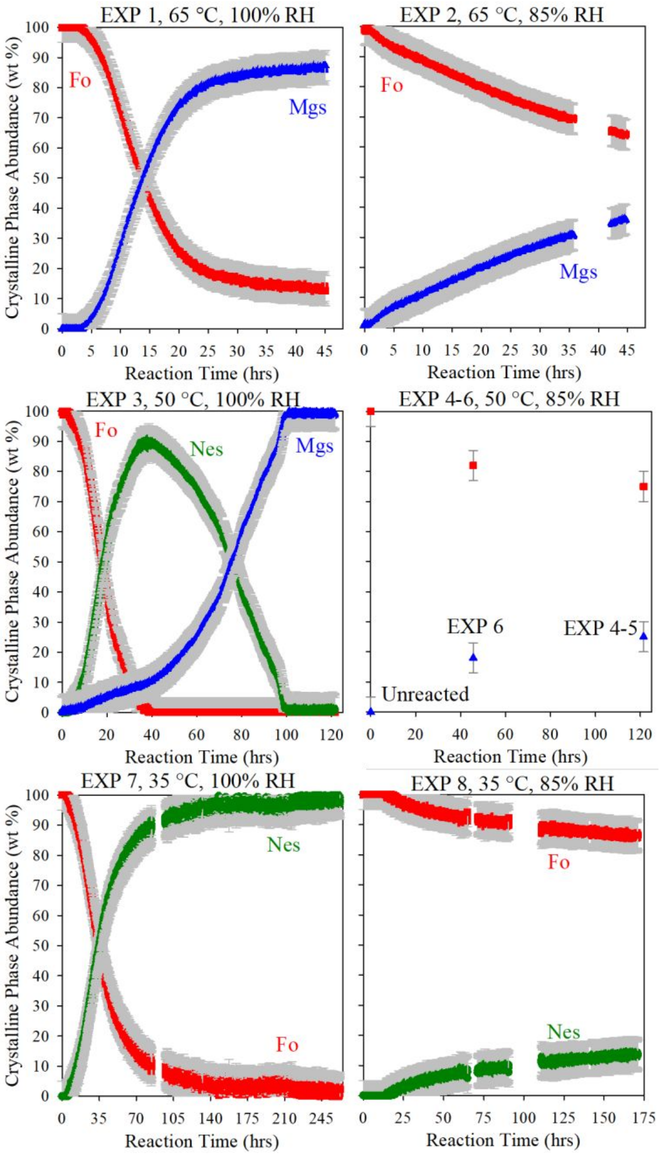

Fig. 3. Time-resolved crystalline mineral abundance plots for EXP 1-8 showing forsterite (Fo, red squares) dissolution and magnesite (Mgs, blue triangles) and/or nesquehonite (Nes, green circles) precipitation at 35-65 °C and 90 atm scCO$_2$ at 100% or 85% RH. *In situ* XRD uncertainty is shown by the grey error bar envelopes around the mineral abundance profiles that have overlapping symbols. The middle right panel shows *ex situ* (TGA-MS) magnesite abundances for the unreacted forsterite and **EXP 4-6** (50/85). All other panels (**EXP 1-3** and **EXP 7-8**) show *in situ* XRD results. Absolute abundances of forsterite used for kinetics calculations are shown in **Fig. S2**.

2.4 Carbonation kinetics calculations

The kinetic model fits and calculations, along with experimentally-validated[62, 65] absolute phase abundance mass balances, are described in detail in Miller et al.[62]. Briefly, the crystalline phase abundances were corrected to account for amorphous silica precipitation according to **Reaction 1** or **2** and then converted into absolute abundances (moles). As shown in **Fig. S2** and tabulated in **Table S1**, the *in situ* XRD time series of decreasing forsterite abundances were fit to first order exponential decay expressions:

$$Q_t=Q_i e^{-kt} \tag{4}$$

where Q_t is the amount of forsterite at time t, Q_i is the initial amount of forsterite, and k is the rate constant (s^{-1}). The rate constant uncertainties are conservatively estimated to be ±10% (**Table S1**), at least 10 times the calculated errors in the kinetic model fits. Although this experimental system may be accurately described with either first order silicate decay[62] or carbonate growth[65] models, in this work we chose to model first order decay (forsterite dissolution), as this model facilitates comparisons between experiments with contrasting reaction extents. The first order rate constants for forsterite dissolution describe the overall carbonation reaction due to the tightly coupled nature of forsterite dissolution and Mg-carbonate precipitation in nanoscale water films [62]. Therefore, in this work, forsterite carbonation and Mg-carbonate precipitation may be used interchangeably. The *ex situ* TGA-MS quantifications of magnesite abundance for **EXP 4-6** were used to calculate the 50/85 carbonation rate constant, because the nanocrystalline magnesite could be detected but not quantified with *in situ* XRD. Due to the fit of the kinetic model (**Table S1**) and the low number of data points relative to other experiments, the uncertainty of the 50/85 rate constant was ~±24%. Although the same forsterite was used in each experiment, this approach may be applied to other particle sizes, as grain size has no significant effects on Mg/Ca-silicate mineral carbonation kinetics if reaction rates are normalized using specific surface areas[73, 91].

The rate constants from the experiments were then used to calculate the apparent activation energies (E_a) of forsterite carbonation under varying degrees of nanoconfinement using the Arrhenius relationship given by:

$$\boldsymbol{k = A_a e^{\frac{-E_a}{RT}}} \tag{5}$$

where R is the gas constant, T is the absolute temperature, and A_a designates a pre-exponential factor. Our calculated E_a values are apparent activation energies because they describe contributions of multiple elementary reactions involved in the

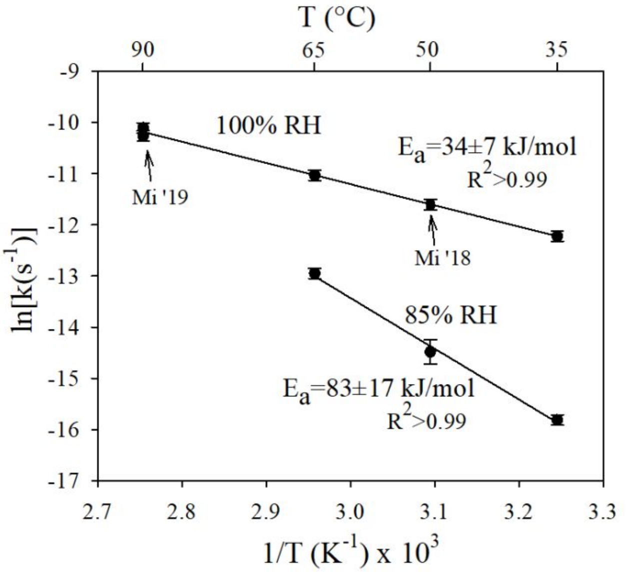

Fig. 4. Arrhenius plot showing the variation of the natural logarithm of the experimentally-derived carbonation rate constants as a function of 1000 times the reciprocal absolute temperature. The calculated apparent activation energies of forsterite carbonation are indicated next to the 100% and 85% RH trend lines. Temperature (°C) is labeled on the upper x-axis for reference. The 100% RH datapoints at 90 °C and 50 °C are from previous studies (see text).[62, 65]

complex dissolution-precipitation processes. Rate constants from this study were plotted on an Arrhenius diagram with the two 90 °C, 89 atm, and 100% RH (90/100) forsterite carbonation rate constants from Miller et al.[62]. The two additional data points were important for parameterizing and extending the 100% RH dataset, as the kinetic model could not be fit to the 50/100 (**EXP 3**) dataset. The Arrhenius plot depicts the natural logarithm of the rate constants as a function of 1000 times the inverse absolute temperature. Lines of best fit were determined with simple linear regression and the negative slopes divided by R resulted in the apparent activation energy of forsterite carbonation in kJ/mol with conservative uncertainties of ±20%.[65]

2.5 Computational methods

The MD simulations used the same model and followed the same approach as described in Kerisit et al.[83] Briefly, the force field combined the SPC/E water model[99], the EPM2 carbon dioxide model[100], and a modified version of CLAYFF[101] for simulating forsterite. The calculations were performed with DL_POLY[102] in the NVT ensemble (constant number of particles, constant volume, and constant temperature) at 50 °C. The (010) forsterite, one of the most stable forsterite surfaces, was chosen to be consistent with the Kerisit et al.[83] study. The forsterite slab was 30-Å thick with a surface area of 28.418 × 29.961 Å^2. The system was periodic in three dimensions, and the scCO$_2$/H$_2$O mixture was contained in a 100-Å gap introduced between the two faces of the forsterite slab.

Three water coverages were considered: 3, 4, and 10 ML. The 3-and 10-ML systems were taken from Kerisit et al.[83]. The 4-ML system was created by removing H$_2$O molecules from and introducing CO$_2$ molecules in the 10-ML system and performing a 1-ns equilibration simulation. Then, in each of the three systems, a Mg^{2+} ion was introduced close to the forsterite surface in an inner-sphere (IS) configuration, and a 1-ns simulation was performed, during which the Mg^{2+} ion remained adsorbed as an IS complex. The final configurations were used as starting points for a first series of potential of mean force (PMF) calculations that extended to 12 Å away from the forsterite surface along the normal to the surface with 0.2-Å intervals. The resulting PMF profiles allowed for identifying the vertical positions of the three outer-sphere (OS) complexes (see section 3.2). A second series of PMF calculations was then run in the direction parallel to the rows of surface Mg^{2+} ions for each of the three OS complexes to determine the free energy barriers for diffusion across the surface (Mg diffusion perpendicular to the rows of surface Mg^{2+} ions was assumed to be associated with larger energy barriers). The individual PMF calculations were run for 400 ps following a 50 ps equilibration period.

3. Results and discussion

3.1 Experimentally-resolved carbonation kinetics and pathways

Results from *in situ* XRD experiments at 35-65 °C were used to determine how adsorbed water film thickness and temperature influenced the carbonation rates and pathways (i.e., precipitation of metastable and/or transient intermediate phases).

At 65 °C, the conversion of forsterite to magnesite (PDF #8-0479) was monitored for the 100 (**EXP 1**) and 85% (**EXP 2**) RH conditions with *in situ* XRD (**Fig. 3**) Forsterite carbonation was rapid for 65/100, with 87 wt % magnesite present after 45 hours, which corresponds to a corrected abundance of 67 wt % and a reaction extent of 91%. SEM (**Fig. 2**) and TGA-MS (**Fig. S3**) results were consistent with magnesite precipitation. The calculated rate constant for 65/100 was 1.61x10^{-5} s^{-1}. In contrast, a decrease in adsorbed water film thicknesses via a 15% reduction in scCO$_2$ water content, from 0.608 to 0.517 mol % (**Table S1**), decreased the carbonation rate of 65/85, resulting in a reaction extent of only 43% after ~45 hours. Relative to the 65/100 rate constant, the carbonation rate constant for 65/85 decreased by 85%, to 2.37x10^{-6} s^{-1}, and both values are shown on the Arrhenius plot (**Fig. 4**).

A similar decrease in carbonation extent due to a decrease in water film thickness was observed at 50 °C for the 50/100 (**EXP 3**) and 50/85 (**EXP 4-6**) experiments. During the ~121 hour 50/100 experiment, forsterite carbonated to magnesite via a nesquehonite intermediate (PDF #20-0669, **Fig. 1**, **Fig. 3**). Absolute abundances, and therefore a rate constant, could not be determined due to the simultaneous appearance of Mg-carbonate phases with distinct molecular weights (magnesite and nesquehonite), which changed the total sample mass in a nonlinear, unconstrained manner. The predicted rate constant for 50/100, based on interpolation of the 100% RH rate constants was 9.19x10^{-6} s^{-1}. This interpolated value is close to the Miller et al.[62] value of 9.10x10^{-6} s^{-1} determined when citrate organic ligands were present to suppress nesquehonite formation (**Fig. S2**).

The carbonation rate constant for 50/85 also could not be calculated using *in situ* XRD data. Although evidence of magnesite precipitation was observed using *ex situ* SEM-EDS (**Fig. 2**), TGA-MS, (**Fig. S3**), high-angle ex situ XRD (**Fig. S4)**, and differential XRD (DXRD, **Fig. S5** and **Fig. S6**), the amount of magnesite could not be quantified using full pattern fitting of *in situ* diffractograms. Quantification was problematic due to the nanocrystalline nature of the magnesite crystallites, as the expanded lattice parameters[103, 104] of the precipitates caused the primary magnesite peak ostensibly at ~32.6 °2*ϑ* to shift and overlap even more with the adjacent forsterite peak at ~32.3 °2*ϑ*. However, *ex situ* TGA-MS abundances for **EXP 4-6** were used to calculate a 50/85 carbonation rate constant of 5.15x10^{-7} s^{-1}, a 94% decrease in rate compared to the predicted 50/100 value. No indications of nesquehonite were observed in the 50/85 (**EXP 4-6**) experiments, indicating the lower water activity of the thinner water film was not conducive to precipitation or stability of nesquehonite. These results concerning nesquehonite-magnesite stability are consistent with the results of previous <87% RH scCO$_2$ forsterite carbonation experiments conducted at 50 C and 89 atm.[63, 74] The change in carbonation pathway between 100% and 85% RH at 50 °C involving the appearance of metastable and/or transient Mg-carbonate precipitation highlights the sensitivity of the system to interfacial water activity and is further discussed in section 3.3.

The final two experiments, conducted at 35 °C, namely 35/100 (**EXP 7**) and 35/85 (**EXP 8**), resulted in nesquehonite precipitation (**Fig. 2**) and no evidence of magnesite precipitation (**Fig. 3, Fig. S1**). The calculated rate constants for 35/100 and 35/85 were 4.92x10^{-6} s^{-1} and 1.35x10^{-7} s^{-1}, respectively (**Table S1**). After 171.1 hours of reaction for 35/100, *in situ* XRD results suggested that ~99 crystalline wt % nesquehonite was present, but only ~14 crystalline wt % nesquehonite precipitated in the same amount of time for the 35/85 experiment. The 35/100 reaction was continued for ~91 additional hours, but the abundance of nesquehonite remained constant and no evidence of magnesite was observed. The appearance and growth of reflections corresponding to nesquehonite in **EXP 8** (35/85) was best visualized by *in situ* DXRD (**Fig. S7**) A 10 wt % discrepancy between carbonation extent for corrected *in situ* XRD and TGA-MS (**Table S1**, **Fig. S3**) for **EXP 8** possibly indicated that amorphous Mg-carbonate[86] and/or magnesite was present in the 35/85 sample. *Ex situ* XRD (**Fig. S4**) analysis of the reacted sample was inconclusive due to the numerous potential overlaps of abundant nesquehonite peaks and magnesite reflections, in addition to the magnesite and forsterite peak overlap.

A prominent result for all experiments conducted at 85-100% RH is that although the reaction rates were lower at 85% RH, continuous carbonation was occurring (**Fig. 3**), with no indication of inhibited reactivity due to formation of Si-rich layers on forsterite, whose properties we have recently discussed in detail.[91] As summarized in that work, Fe-free Mg$_2$SiO$_4$ dissolution and/or carbonation has not been demonstrated to be inhibited by Si-rich layer formation, due to the important role of iron redox reactions in determining the properties of secondary coatings.[91] The lack of reaction-limiting armouring by Si-rich layers during Fe-free forsterite carbonation[91] that would require a reacted layer diffusion kinetic model[105] is also consistent with the results of ^{29}Si nuclear magnetic resonance (NMR) spectroscopy forsterite carbonation studies[71, 93] that demonstrated the formation of highly-porous amorphous silica. Lastly, as discussed by Min et al.[73], possible anisotropic reactivity for different crystal faces (i.e. ref [106]) does not appear to control reaction extent or kinetics.

3.2 Molecular insights into ion diffusion origins of reactivity thresholds

MD simulations of Mg^{2+} diffusivities at the H$_2$O-scCO$_2$-forsterite interface provided new molecular-scale mechanistic insight into how water film thickness could influence nanoconfined reactivity thresholds. PMF calculations for the 3, 4, and 10 ML H$_2$O coverage simulations identified one IS and three OS Mg^{2+} complexes at the (010) surface of forsterite (**Fig. 5a-b**). The IS complex is bound to three surface oxygens and three water molecules. OS 1 is positioned in the centre of the grooves formed by the rows of surface Mg^{2+} ions, and three of its first-shell H$_2$O molecules donate hydrogen bonds to surface oxygens. OS 2 is also positioned in the surface grooves but in an off-centre position; one of its first-shell H$_2$O molecules is shared with a surface Mg^{2+} and another two donate hydrogen bonds to surface oxygens. OS 3 is positioned further away from the surface with one or two of its first-shell H$_2$O molecules involved in hydrogen bonding with adsorbed H$_2$O molecules.

The IS complex is very strongly bound to the surface and is not expected to diffuse on the timescale of the experiments (**Fig. 5b**). The calculated densities of H$_2$O (**Fig. 5c**) for the three coverages are consistent with the results of Kerisit et al.[83] The PMF calculations in the direction parallel to the surface rows (**Fig. 5d**) showed that steep energy barriers are associated with moving OS 1 and 2 along the surface grooves. In contrast, because it is more loosely bound to the surface, OS 3 only has to escape shallow energy minima to diffuse across the surface. However, there is no metastable OS 3 configuration above the OS 1 site, which signifies that OS 3 will relax down to OS 1 when it reaches this site. Importantly, the interval between two OS 1 sites is approximately 4.7 Å due to the periodicity of the forsterite surface lattice. As a result, an OS Mg^{2+} ion must go through OS 3 in order to reach the next OS 1 and OS 2 sites and thus diffuse across the surface. Because OS 3 is further away from the surface and is thus involved extensively in hydrogen bonding with water molecules in the fourth layer, its free energy relative to OS 1 and 2 is very sensitive to the water coverage at low coverages. Specifically, the PMF calculations

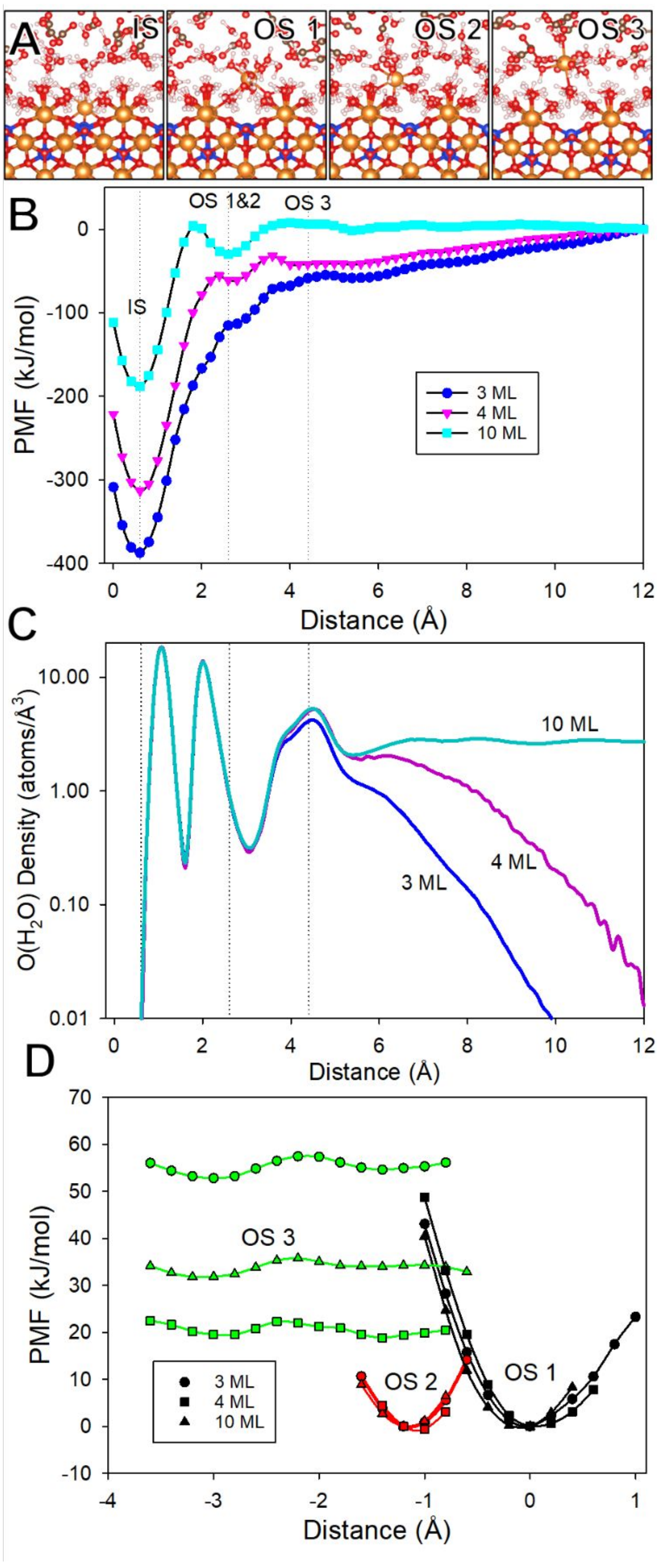

Fig. 5. (a) Snapshots of the inner sphere (IS) and outer sphere (OS) Mg^{2+} complexes. (b) Potential of mean force for a Mg^{2+} ion approaching the (010) forsterite surface as a function of water coverage. (c) O(H_2O) density profiles as a function of distance away from the (010) forsterite surface. Dotted grey reference lines in (b) and (c) denote IS and OS positions. (d) Potential of mean force for a Mg^{2+} ion moving along the surface grooves (direction perpendicular to the plane of the images shown in (a)) as a function of water coverage.

predict that OS 3 is stabilized by approximately 35 kJ/mol as the water coverage increases from 3 ML to 4 ML (**Fig. 5d**). The resulting significant decrease in free energy barrier for the OS 1-OS 3 transition indicates that at least 4 MLs are needed to allow for the diffusion of Mg^{2+} across the surface as an OS complex. Because diffusion of Mg^{2+} is required to form Mg carbonate products, the MD simulations therefore predict the presence of a reactivity threshold between 3 and 4 ML for the formation of any Mg carbonate product. Although MD simulations considered one Mg^{2+} diffusing in the interfacial water film, as we are interested in the incipient stages of carbonation, it is possible that other Mg^{2+} ions may change the free energy landscape of diffusion. However, saturation of IS or OS sites by Mg^{2+} would require forsterite dissolution that is not favoured until a critical water coverage is obtained.

In order to correlate experimental and computational results, previous experimental determinations of water film thicknesses at different 50 °C RH conditions[63] were used in conjunction with MD simulation-derived parameters from Kerisit et al.[83, 107] for the (010) forsterite surface, to calculate a forsterite water film thickness and monolayer coverage for the 100% and 85% RH conditions at 50 °C. The water film thickness at 100% RH is 0.92 nm and at 85% RH it is 0.64 nm, which correspond to 5.0 and 3.6 ML of water, respectively (Table S2), assuming the water films are of uniform thickness. These thickness values represent approximate, likely minimal, relevant coverages, as the forsterite nanoparticles were not exposed to vacuum and may host up to 2 ML of water at initial ambient conditions[108]. Even the nominally dry forsterite sample prior to CO_2 exposure has detectable sorbed water and (bi)carbonate.[63, 76, 94], and capillary water, water-water interactions, hydrophilic solutes, and defect sites may contribute to water film thickening [84, 109-112], although water condensation is likely negligible due to the scarcity of interparticle volume for submicron-sized particles[113]. If we consider that the experimental ML values are added to the forsterite surface, which may host 1-2 ML of H_2O, MD simulations and experimental results appear to be in good quantitative agreement. For example, the experimentally-determined water film thickness on forsterite at the 70% RH reactivity threshold is ~2.4 ML (~0.42 nm, Table S2)[63] added to 1-2 ML, for a combined thickness of ~3.4-4.4 ML, and our molecular simulations indicate a transport threshold occurs between 3-4 ML for the (010) forsterite surface. This result strongly suggests mineral reactivity thresholds in nanoscale adsorbed water films could be a direct consequence of solute mobility and transport.

3.3 Nanoconfined carbonation kinetics in the context of ion hydration and diffusion

The *in situ* XRD mineral abundance profiles demonstrate that greater nanoconfinement in thinner interfacial water films reduced forsterite carbonation rates by ~85% at 65 °C to ~97% at 35 °C. The resultant apparent activation energies of carbonation for the 100% and 85% RH conditions were 34±7 and 83±17 kJ/mol, respectively (**Fig. 4**). The strong dependence of mineralization kinetics on water film thickness from 85-100% RH has not previously been quantified. In this RH region, we suggest that the increasing water coverage enabling lateral Mg^{2+} diffusion is responsible for the observed reduction in carbonation activation energy. Ion diffusion rates are inhibited in nanoconfined environments, including in water films, interlayers, and pores.[37, 39, 114-116] These slower rates of solute diffusion may potentially impact all constituent reactions of forsterite dissolution and Mg-carbonate precipitation. Our results are broadly consistent with previous work examining the mobility of ions through unsaturated porous geomedia such as sand, rocks, as well as cementitious materials at room temperature. These workers observed strongly-inhibited (>10x) ion diffusion rates at 85% saturated conditions.[37, 117, 118]

As highlighted in Miller et al.[65], the apparent activation energy for magnesite precipitation in ~1 nm-thick water films at 100% RH is substantially lower than the value for magnesite precipitation in bulk water (~103 kJ/mol[65, 119-125]), likely due to the reduced dielectric constant that leads to a greater proportion of less-strongly hydrated Mg^{2+} cations, conditions favourable for anhydrous Mg-carbonate precipitation. The promotion of magnesite and suppression of nesquehonite at 50/85 compared to the thicker film 50/100 condition, which has not been previously demonstrated, is particularly illustrative of how nanoconfinement may affect the inner sphere coordination environment of Mg^{2+}. Anhydrous Mg-carbonate precipitation requires the removal of all six waters that typically coordinate the magnesium cation[126-131], and the reduced ability of nanoconfined water to solvate Mg^{2+} lowers this kinetic barrier by ~50 kJ/mol[65]. Studies have also demonstrated enhanced Mg^{2+} dehydration may be facilitated by competitive complexation to (bi)carbonate[129] or organic ligands[61, 62, 132, 133]. More recent research has shown that hydrated Mg^{2+} complexes may be weakened by interactions with clay mineral[134] or carbonate[135] surfaces, promoting the nucleation and growth of anhydrous Mg-carbonates. Overall, the 50 °C experiments demonstrate that Mg-carbonate phase stabilities may be used as a sensitive geochemical indicator of interfacial water activity.

In the context of Miller et al.[65], the current results are suggestive of a nonmonotonic dependence of carbonation kinetics on the degree of confinement (water film thickness) from bulk water conditions to <1 nm-thick adsorbed water films at 85% RH. This experimentally-resolved regime may reflect a change in rate limiting processes between (de)hydration and diffusion processes. Magnesite precipitation in a “thick” (100% RH) nanoscale water film may be favoured relative to bulk aqueous conditions due to the less-strongly hydrated Mg^{2+} cation[65,] but continuing decreases in water film thickness results in slower reaction kinetics and increased apparent activation energy of Mg-carbonate growth due the inhibition of solute diffusion in more structured thinner water film, as conceptually illustrated in **Fig. S8**. This concept of competition between thermodynamic and kinetic effects is exemplified by the work of Li and Jun[136], who demonstrated that increasing salinity promotes calcium carbonate nucleation via a reduction in interfacial energy while also reducing the kinetics of monomer attachment to nuclei. More research is needed to examine our present hypothesis in detail. Currently, it is unclear if other mechanisms, including those operating in microdroplets[137] and at fluid/gas interfaces[138], play important roles in nanoconfined carbonation reaction trends, and additional theoretical investigations and continued development of high-pressure *in situ* interfacial probes are required to further clarify. Nonetheless, a general implication from the findings to date is that RH control indeed represents a potent system variable that can be used to optimize water film thicknesses, resulting reactions rates, and, in principle, the efficacy of carbon storage in the subsurface.

3.4 Environmental implications

Based on the apparent activation energies of the 100 and 85% RH conditions, slowing of mineral transformation rates due to nanoconfinement will be less pronounced at higher temperature metamorphic and diagenetic conditions, and relatively more impactful in low temperature settings that compose the critical zone, including soils[2], regolith[139], and atmospheric dust[9]. The enhanced inhibition of reaction rates at low temperatures due to confinement conceivably may also be partly responsible for the well-known discrepancy between field- and laboratory-derived weathering rates[140], as speculated by Wang et al. [4]. Additionally, nanoscale interfacial water films that are chemically and physically distinct from the bulk fluid phase form at hydrophilic mineral surfaces [141, 142] and have been demonstrated to control silicate dissolution and precipitation.[143-145] As uniquely structured fluids are present at solid interfaces even in ostensibly bulk fluid environments, our results have widespread implications for predicting rates of many transformations at environmental and technological interfaces.

4. Conclusions

Coupled experiments and molecular modelling showed that the carbonation kinetics of forsterite exposed to $scCO_2$ at 35-65 °C and 100 or 85% RH may have at least a partial mechanistic basis in mass transfer rates in thin water films. Decreasing the water film thickness by ~1.4 ML, from ~0.92 to ~0.64 nm, inhibited reaction rates by up to 97%, promoted anhydrous Mg-carbonate precipitation, and more than doubled the apparent activation energy of carbonation. MD simulations performed to determine the free energy landscape of Mg^{2+} adsorption and diffusion on forsterite (010) surfaces as a function of water film thickness revealed that four monolayers of adsorbed water are required to allow Mg^{2+} to diffuse across the surface at rates sufficient to sustain carbonation, helping explain the previously unknown mechanisms responsible for water-dependent reactivity thresholds. Our study adds to existing knowledge by pointing to the prospective importance of mass transfer kinetics determining rates and reactivity thresholds at complex hydrated interfaces in rocks, soil, and other porous media.

Conflicts of interest

There are no conflicts to declare.

Author ORCID Information

QRSM: 0000-0003-3009-9702
JPK: 0000-0001-8799-0673
SNK: 0000-0002-7470-9181
HTS: 0000-0002-4546-3979
MEB: 0000-0003-3812-3340
KMR: 0000-0002-8474-7720

Acknowledgements

This material is based on work supported by the U.S. Department of Energy (DOE), Office of Science, Office of Basic Energy Sciences (BES), Chemical Sciences, Geosciences, and Biosciences Division through its Geosciences program at Pacific Northwest National Laboratory (PNNL). This BES program supported the activities of QRSM, SNK, and KMR. JPK was supported by the University of Wyoming School of Energy Resources and a Nielson Energy Fellowship. HTS, MEB, and BPM were supported by the U.S. Department of Energy Office of Fossil Energy at PNNL through the National Energy Technology Laboratory, Morgantown, West Virginia. QRSM acknowledges initial support by the University of Wyoming (UW) Department of Geology and Geophysics and School of Energy Resources. A portion of this work was performed at the Environmental and Molecular Sciences Laboratory (EMSL), a national scientific user facility at PNNL that is managed by the DOE's Office of Biological and Environmental Research. We thank Sean Scott, Carrick Eggleston, and PNNL's Geochemistry team for helpful discussions and reviews. We also thank Odeta Qafoku for SEM-EDS imaging, John Loring for forsterite synthesis, and Dushyant Barpaga for MATLAB waterfall plot script development. Lastly, we thank the two anonymous peer reviewers, whose insight and attention have helped improve the manuscript.

References

1. M. J. Molina, Polar Ozone Depletion (Nobel Lecture), *Angewandte Chemie International Edition in English*, 1996, **35**, 1778-1785.
2. J. Zachara, S. Brantley, J. Chorover, R. Ewing, S. Kerisit, C. X. Liu, E. Perfect, G. Rother and A. G. Stack, Internal Domains of Natural Porous Media Revealed: Critical Locations for Transport, Storage, and Chemical Reaction, *Environ. Sci. Technol.*, 2016, **50**, 2811-2829.
3. O. Plumper, A. Botan, C. Los, Y. Liu, A. Malthe-Sorenssen and B. Jamtveit, Fluid-driven metamorphism of the continental crust governed by nanoscale fluid flow, *Nat. Geosci.*, 2017, **10**, 685.
4. Y. F. Wang, C. Bryan, H. F. Xu and H. Z. Gao, Nanogeochemistry: Geochemical reactions and mass transfers in nanopores, *Geology*, 2003, **31**, 387-390.
5. J. Nelson, J. R. Bargar, L. Wasylenki, G. E. Brown and K. Maher, Effects of nano-confinement on Zn(II) adsorption to nanoporous silica, *Geochim. Cosmochim. Acta*, 2018, **240**, 80-97.
6. C. R. Usher, A. E. Michel and V. H. Grassian, Reactions on mineral dust, *Chem. Rev.*, 2003, **103**, 4883-4939.
7. Y. Wang, Nanogeochemistry: Nanostructures, emergent properties and their control on geochemical reactions and mass transfers, *Chem. Geol.*, 2014, **378–379**, 1-23.
8. Y. Wang, G. Huizhen and H. Xu, in *Frontiers in Geochemistry: Contribution of Geochemistry to the Study of the Earth*, eds. R. S. Harmon and A. Parker, Wiley Blackwell, 2011, ch. 10, pp. 200-220.
9. G. Rubasinghege and V. H. Grassian, Role(s) of adsorbed water in the surface chemistry of environmental interfaces, *Chem. Commun.*, 2013, **49**, 3071-3094.
10. A. Kereszturi and S. Gobi, Possibility of H_2O_2 decomposition in thin liquid films on Mars, *Planet. Space Sci.*, 2014, **103**, 153-166.
11. F. J. Martin-Torres, M. P. Zorzano, P. Valentin-Serrano, A. M. Harri, M. Genzer, O. Kemppinen, E. G. Rivera-Valentin, I. Jun, J. Wray, M. B. Madsen, W. Goetz, A. S. McEwen, C. Hardgrove, N. Renno, V. F. Chevrier, M. Mischna, R. Navarro-Gonzalez, J. Martinez-Frias, P. Conrad, T. McConnochie, C. Cockell, G. Berger, A. R. Vasavada, D. Sumner and D. Vaniman, Transient liquid water and water activity at Gale crater on Mars, *Nat. Geosci.*, 2015, **8**, 357-361.
12. C. S. Boxe, K. P. Hand, K. H. Nealson, Y. L. Yung, A. S. Yen and A. Saiz-Lopez, Adsorbed water and thin liquid films on Mars, *IJAsB*, 2012, **11**, 169-175.
13. T. K. Tokunaga, Physicochemical controls on adsorbed water film thickness in unsaturated geological media, *Water Resour. Res.*, 2011, **47**, W08514.
14. N. C. Osti, M. Naguib, A. Ostadhossein, Y. Xie, P. R. C. Kent, B. Dyatkin, G. Rother, W. T. Heller, A. C. T. van Duin, Y. Gogotsi and E. Mamontov, Effect of metal ion intercalation on the structure of MXene and water dynamics on its internal surfaces, *ACS Appl. Mater. Interfaces*, 2016, **8**, 8859-8863.
15. A. Paciaroni, M. Casciola, E. Cornicchi, M. Marconi, G. Onori, M. Pica and R. Narducci, Temperature-dependent dynamics of water confined in nafion membranes, *J. Phys. Chem. B.*, 2006, **110**, 13769-13776.
16. Y. Zhu, Y. Ruan, Y. Zhang, L. Lu and X. Lu, Nanomaterial-oriented molecular simulations of ion behaviour in aqueous solution under nanoconfinement, *Mol. Sim.*, 2016, **42**, 784-798.
17. D. Cipolla, H. Wu, S. Salentinig, B. Boyd, T. Rades, D. Vanhecke, A. Petri-Fink, B. Rothin-Rutishauser, S. Eastman, T. Redelmeier, I. Gonda and H. K. Chan, Formation of drug nanocrystals under nanoconfinement afforded by liposomes, *RSC Adv.*, 2016, **6**, 6223-6233.
18. J. Bohr, R. A. Wogelius, P. M. Morris and S. L. S. Stipp, Thickness and structure of the water film deposited from vapour on calcite surfaces, *Geochim. Cosmochim. Acta*, 2010, **74**, 5985-5999.
19. A. G. Kalinichev, J. Wang and R. J. Kirkpatrick, Molecular dynamics modeling of the structure, dynamics and energetics of mineral–water interfaces: Application to cement materials, *Cem. Concr. Res.*, 2007, **37**, 337-347.

20. A. Striolo, Interfacial water studies and their relevance for the energy sector, *Mol. Phys.*, 2016, **114**, 2615-2626.
21. A. Yethiraj and A. Striolo, Fracking: What Can Physical Chemistry Offer?, *J. Phys. Chem. Lett.*, 2013, **4**, 687-690.
22. A. G. Ilgen, J. E. Heath, I. Y. Akkutlu, L. T. Bryndzia, D. R. Cole, Y. K. Kharaka, T. J. Kneafsey, K. L. Milliken, L. J. Pyrak-Nolte and R. Suarez-Rivera, Shales at all scales: Exploring coupled processes in mudrocks, *Earth-Sci. Rev.*, 2017, **166**, 132-152.
23. S. Gin, P. Jollivet, M. Fournier, F. Angeli, P. Frugier and T. Charpentier, Origin and consequences of silicate glass passivation by surface layers, *Nat. Comm.*, 2015, **6**, 6360.
24. I. C. Bourg, G. Sposito and A. C. M. Bourg, Tracer diffusion in compacted, water-saturated bentonite, *Clays Clay Miner.*, 2006, **54**, 363-374.
25. D. Muñoz-Santiburcio and D. Marx, Chemistry in nanoconfined water, *Chem. Sci.*, 2017, **8**, 3444-3452.
26. L. B. Williams, J. R. Holloway, B. Canfield, C. R. Glein, J. M. Dick, H. E. Hartnett and E. L. Shock, in *Earliest Life on Earth: Habitats, Environments and Methods of Detection*, eds. S. D. Golding and M. Glikson, Springer Netherlands, Dordrecht, 2011, DOI: 10.1007/978-90-481-8794-2_4, pp. 79-112.
27. C. J. Stephens, S. F. Ladden, F. C. Meldrum and H. K. Christenson, Amorphous calcium carbonate is stabilized in confinement, *Adv. Funct. Mater.*, 2010, **20**, 2108-2115.
28. D. Kim, B. Lee, S. Thomopoulos and Y.-S. Jun, The role of confined collagen geometry in decreasing nucleation energy barriers to intrafibrillar mineralization, *Nat. Comm.*, 2018, **9**, 962.
29. D. Argyris, N. R. Tummala, A. Striolo and D. R. Cole, Molecular Structure and Dynamics in Thin Water Films at the Silica and Graphite Surfaces, *J. Phys. Chem. C*, 2008, **112**, 13587-13599.
30. J. G. Catalano, Relaxations and Interfacial Water Ordering at the Corundum (110) Surface, *J. Phys. Chem. C*, 2010, **114**, 6624-6630.
31. A. W. Knight, N. G. Kalugin, E. Coker and A. G. Ilgen, Water properties under nano-scale confinement, *Sci. Rep.*, 2019, **9**, 8246.
32. O. Teschke, G. Ceotto and E. F. de Souza, Interfacial water dielectric-permittivity-profile measurements using atomic force microscopy, *PhRvE*, 2001, **64**, 011605.
33. S. Senapati and A. Chandra, Dielectric constant of water confined in a nanocavity, *J Phys Chem B*, 2001, **105**, 5106-5109.
34. L. Fumagalli, A. Esfandiar, R. Fabregas, S. Hu, P. Ares, A. Janardanan, Q. Yang, B. Radha, T. Taniguchi and K. Watanabe, Anomalously low dielectric constant of confined water, *Science*, 2018, **360**, 1339-1342.
35. S. De Luca, S. K. Kannam, B. D. Todd, F. Frascoli, J. S. Hansen and P. J. Daivis, Effects of confinement on the dielectric response of water extends up to mesoscale dimensions, *Langmuir*, 2016, **32**, 4765-4773.
36. J. A. Greathouse, R. T. Cygan, J. T. Fredrich and G. R. Jerauld, Molecular Dynamics Simulation of Diffusion and Electrical Conductivity in Montmorillonite Interlayers, *J. Phys. Chem. C*, 2016, **120**, 1640-1649.
37. T. K. Tokunaga, S. Finsterle, Y. Kim, J. Wan, A. Lanzirotti and M. Newville, Ion Diffusion Within Water Films in Unsaturated Porous Media, *Environ. Sci. Technol.*, 2017, **51**, 4338-4346.
38. I. C. Bourg and C. I. Steefel, Molecular Dynamics Simulations of Water Structure and Diffusion in Silica Nanopores, *The Journal of Physical Chemistry C*, 2012, **116**, 11556-11564.
39. S. Kerisit and C. Liu, Molecular Simulations of Water and Ion Diffusion in Nanosized Mineral Fractures, *Environ. Sci. Technol.*, 2009, **43**, 777-782.
40. Q. Jiang and M. D. Ward, Crystallization under nanoscale confinement, *Chem. Soc. Rev.*, 2014, **43**, 2066-2079.
41. C. Anduix-Canto, Y. Y. Kim, Y. W. Wang, A. Kulak, F. C. Meldrum and H. K. Christenson, Effect of nanoscale confinement on the crystallization of potassium ferrocyanide, *Cryst. Growth Des.*, 2016, **16**, 5403-5411.
42. C. J. Stephens, Y.-Y. Kim, S. D. Evans, F. C. Meldrum and H. K. Christenson, Early stages of crystallization of calcium carbonate revealed in picoliter droplets, *J. Am. Chem. Soc.*, 2011, **133**, 5210-5213.
43. Y. Wang, M. Zeng, F. C. Meldrum and H. K. Christenson, Using confinement to study the crystallization pathway of calcium carbonate, *Cryst. Growth Des.*, 2017, **17**, 6787-6792.
44. D. B. Hausner, R. J. Reeder and D. R. Strongin, Humidity-induced restructuring of the calcite surface and the effect of divalent heavy metals, *J. Colloid Interface Sci.*, 2007, **305**, 101-110.
45. Y. Diao and R. M. Espinosa-Marzal, The role of water in fault lubrication, *Nat. Comm.*, 2018, **9**, 2309.
46. L. Ma, A. Gaisinskaya-Kipnis, N. Kampf and J. Klein, Origins of hydration lubrication, *Nat. Comm.*, 2015, **6**, 6060.
47. Z. Li, G. Jeanmairet, T. Méndez-Morales, M. Burbano, M. Haefele and M. Salanne, Confinement Effects on an Electron Transfer Reaction in Nanoporous Carbon Electrodes, *J. Phys. Chem. Lett.*, 2017, **8**, 1925-1931.
48. R. C. Remsing, I. G. McKendry, D. R. Strongin, M. L. Klein and M. J. Zdilla, Frustrated Solvation Structures Can Enhance Electron Transfer Rates, *J. Phys. Chem. Lett.*, 2015, **6**, 4804-4808.
49. S. Patra, A. K. Pandey, S. K. Sarkar and A. Goswami, Wonderful nanoconfinement effect on redox reaction equilibrium, *RSC Adv.*, 2014, **4**, 33366-33369.
50. A. W. Knight, A. B. Tigges and A. G. Ilgen, Adsorption of copper (II) on mesoporous silica: the effect of nano-scale confinement, *Geochem. Trans.*, 2018, **19**, 13.
51. C. P. Schulthess, R. W. Taylor and D. R. Ferreira, The Nanopore Inner Sphere Enhancement Effect on Cation Adsorption: Sodium and Nickel, *SSSAJ*, 2011, **75**, 378-388.
52. A. W. Knight, P. Ilani-Kashkouli, J. A. Harvey, J. A. Greathouse, T. A. Ho, N. Kabengi and A. G. Ilgen, Interfacial reactions of Cu(ii) adsorption and hydrolysis driven by nano-scale confinement, *Environ. Sci. Nano*, 2020, **7**, 68-80.
53. G. Rother, E. G. Krukowski, D. Wallacher, N. Grimm, R. J. Bodnar and D. R. Cole, Pore Size Effects on the Sorption of Supercritical CO_2 in Mesoporous CPG-10 Silica, *J. Phys. Chem. C*, 2012, **116**, 917-922.
54. T. Le, A. Striolo, C. H. Turner and D. R. Cole, Confinement Effects on Carbon Dioxide Methanation: A Novel Mechanism for Abiotic Methane Formation, *Sci. Rep.*, 2017, **7**, 9021.
55. B. P. Wiebenga-Sanford, J. DiVerdi, C. D. Rithner and N. E. Levinger, Nanoconfinement's dramatic impact on proton

exchange between glucose and water, *J. Phys. Chem. Lett.*, 2016, **7**, 4597-4601.

56. M. E. McBriarty, G. F. von Rudorff, J. E. Stubbs, P. J. Eng, J. Blumberger and K. M. Rosso, Dynamic Stabilization of Metal Oxide–Water Interfaces, *J. Am. Chem. Soc.*, 2017, **139**, 2581-2584.
57. D. Muñoz-Santiburcio, C. Wittekindt and D. Marx, Nanoconfinement effects on hydrated excess protons in layered materials, *Nat. Comm.*, 2013, **4**, 2349.
58. D. Muñoz-Santiburcio and D. Marx, Nanoconfinement in slit pores enhances water self-dissociation, *Phys. Rev. Lett.*, 2017, **119**, 056002.
59. Y. A. P. Sirkin, A. Hassanali and D. n. A. Scherlis, One-Dimensional Confinement Inhibits Water Dissociation in Carbon Nanotubes, *J. Phys. Chem. Lett.*, 2018, **9**, 5029-5033.
60. A. Tsukanov, E. Shilko and S. Psakhie, in *Trigger Effects in Geosystems*, eds. G. Kocharyan and A. Lyakhov, Springer International Publishing, 2019, pp. 297-306.
61. Q. R. S. Miller, J. P. Kaszuba, H. T. Schaef, M. E. Bowden and B. P. McGrail, Impacts of organic ligands on forsterite reactivity in supercritical CO_2 fluids, *Environ. Sci. Technol.*, 2015, **49**, 4724-4734.
62. Q. R. S. Miller, H. T. Schaef, J. P. Kaszuba, L. Qiu, M. E. Bowden and B. P. McGrail, Tunable Manipulation of Mineral Carbonation Kinetics in Nanoscale Water Films via Citrate Additives, *Environmental Science & Technology*, 2018, **52**, 7138-7148.
63. Q. R. S. Miller, D. A. Dixon, S. D. Burton, E. D. Walter, D. W. Hoyt, A. S. McNeill, J. D. Moon, K. S. Thanthiriwatte, E. S. Ilton, O. Qafoku, C. J. Thompson, H. T. Schaef, K. M. Rosso and J. S. Loring, Surface-catalyzed oxygen exchange during carbonation in nanoscale water films, *J. Phys. Chem. C*, 2019, **120**, 12871-12885.
64. Q. R. S. Miller, E. S. Ilton, O. Qafoku, D. A. Dixon, M. Vasiliu, C. J. Thompson, H. T. Schaef, K. M. Rosso and J. S. Loring, Water Structure Controls Carbonic Acid Formation in Adsorbed Water Films, *J. Phys. Chem. Lett.*, 2018, **9**, 4988-4994.
65. Q. R. S. Miller, J. P. Kaszuba, H. T. Schaef, M. E. Bowden, B. P. McGrail and K. M. Rosso, Anomalously low activation energy of nanoconfined $MgCO_3$ precipitation, *Chem. Commun.*, 2019, **55**, 6835-6837.
66. A. Malani, S. Murad and K. G. Ayappa, Hydration of ions under confinement, *Mol. Sim.*, 2010, **36**, 579-589.
67. R. K. Kalluri, D. Konatham and A. Striolo, Aqueous NaCl Solutions within Charged Carbon-Slit Pores: Partition Coefficients and Density Distributions from Molecular Dynamics Simulations, *J. Phys. Chem. C*, 2011, **115**, 13786-13795.
68. J. S. Loring, Q. R. S. Miller, H. T. Schaef and C. J. Thompson, in *Science of Carbon Storage in Deep Saline Formations: Process Coupling across Time and Spatial Scales*, eds. P. Newell and A. G. Ilgen, Elsevier, 1st edn., 2018.
69. J. P. Kaszuba, L. L. Williams, D. R. Janecky, W. K. Hollis and I. N. Tsimpanogiannis, Immiscible CO_2-H_2O fluids in the shallow crust, *Geochem. Geophys. Geosyst.*, 2006, **7(10)**, Q10003.
70. X. Wang, V. Alvarado, N. Swoboda-Colberg and J. P. Kaszuba, Reactivity of dolomite in water-saturated supercritical carbon dioxide: Significance for carbon capture and storage and for enhanced oil and gas recovery, *Energy Convers. Manage.*, 2013, **65**, 564-573.
71. A. R. Felmy, O. Qafoku, B. W. Arey, J. Z. Hu, M. Hu, H. T. Schaef, E. S. Ilton, N. J. Hess, C. I. Pearce, J. Feng and K. M. Rosso, Reaction of water-saturated supercritical CO_2 with forsterite: Evidence for magnesite formation at low temperatures, *Geochim. Cosmochim. Acta*, 2012, **91**, 271-282.
72. O. Qafoku, L. Kovarik, R. K. Kukkadapu, E. S. Ilton, B. W. Arey, J. Tucek and A. R. Felmy, Fayalite dissolution and siderite formation in water-saturated supercritical CO_2, *Chem. Geol.*, 2012, **332**, 124-135.
73. Y. Min, Q. Li, M. Voltolini, T. Kneafsey and Y.-S. Jun, Wollastonite Carbonation in Water-Bearing Supercritical CO_2: Effects of Particle Size, *Environ. Sci. Technol.*, 2017, **51**, 13044-13053.
74. J. S. Loring, J. Chen, P. Benezeth, O. Qafoku, E. S. Ilton, N. M. Washton, C. J. Thompson, P. F. Martin, B. P. McGrail, K. M. Rosso, A. R. Felmy and H. T. Schaef, Evidence for carbonate surface complexation during forsterite carbonation in wet supercritical carbon dioxide, *Langmuir*, 2015, **31**, 7533-7543.
75. Q. R. S. Miller, C. J. Thompson, J. S. Loring, C. F. Windisch, M. E. Bowden, D. W. Hoyt, J. Z. Hu, B. W. Arey, K. M. Rosso and H. T. Schaef, Insights into silicate carbonation processes in water-bearing supercritical CO_2 fluids, *Int. J. Greenhouse Gas Control*, 2013, **15**, 104-118.
76. J. S. Loring, C. J. Thompson, Z. Wang, A. G. Joly, D. S. Sklarew, H. T. Schaef, E. S. Ilton, K. M. Rosso and A. R. Felmy, In situ infrared spectroscopic study of forsterite carbonation in wet supercritical CO_2, *Environ. Sci. Technol.*, 2011, **45**, 6204-6210.
77. B. P. McGrail, H. T. Schaef, V. A. Glezakou, L. X. Dang and A. T. Owen, Water reactivity in the liquid and supercritical CO_2 phase: Has half the story been neglected?, *Energy Procedia*, 2009, **1**, 3415-3419.
78. H. Lin, T. Fujii, R. Takisawa, T. Takahashi and T. Hashida, Experimental evaluation of interactions in supercritical CO_2/water/rock minerals system under geologic CO_2 sequestration conditions, *J. Mater. Sci.*, 2008, **43**, 2307-2315.
79. M. D. Halls and H. B. Schlegel, Chemistry inside carbon nanotubes: the Menshutkin S_N2 reaction, *J. Phys. Chem. B.*, 2002, **106**, 1921-1925.
80. K. Kołodziejczyk, M. Tarnacka, E. Kamińska, M. Dulski, K. Kamiński and M. Paluch, Crystallization Kinetics under Confinement. Manipulation of the Crystalline Form of Salol by Varying Pore Diameter, *Cryst. Growth Des.*, 2016, **16**, 1218-1227.
81. S. Emmanuel, J. J. Ague and O. Walderhaug, Interfacial energy effects and the evolution of pore size distributions during quartz precipitation in sandstone, *Geochim. Cosmochim. Acta*, 2010, **74**, 3539-3552.
82. E. E. Santiso, M. K. Kostov, A. M. George, M. B. Nardelli and K. E. Gubbins, Confinement effects on chemical reactions—Toward an integrated rational catalyst design, *Appl. Surf. Sci.*, 2007, **253**, 5570-5579.
83. S. Kerisit, J. H. Weare and A. R. Felmy, Structure and dynamics of forsterite-scCO_2/H_2O interfaces as a function of water content, *Geochim. Cosmochim. Acta*, 2012, **84**, 137-151.

84. C. J. Thompson, P. F. Martin, J. Chen, P. Benezeth, H. T. Schaef, K. M. Rosso, A. R. Felmy and J. S. Loring, Automated high-pressure titration system with in situ infrared spectroscopic detection, *Rev. Sci. Instrum.*, 2014, **85**, 044102.

85. A. Saberi, B. Alinejad, Z. Negahdari, F. Kazemi and A. Almasi, A novel method to low temperature synthesis of nanocrystalline forsterite, *Mater. Res. Bull.*, 2007, **42**, 666-673.

86. H. T. Schaef, B. P. McGrail, J. L. Loring, M. E. Bowden, B. W. Arey and K. M. Rosso, Forsterite [Mg_2SiO_4] carbonation in wet supercritical CO_2: An in situ high pressure X-ray diffraction study, *Environ. Sci. Technol.*, 2013, **47**, 174-181.

87. H. T. Schaef, C. F. Windisch, Jr., B. P. McGrail, P. F. Martin and K. M. Rosso, Brucite $Mg(OH_2)$ carbonation in wet supercritical CO_2: An *in situ* high pressure X-ray diffraction study, *Geochim. Cosmochim. Acta*, 2011, **75**, 7458-7471.

88. R. D. Springer, Z. Wang, A. Anderko, P. Wang and A. R. Felmy, A thermodynamic model for predicting mineral reactivity in supercritical carbon dioxide: I. Phase behavior of carbon dioxide-water-chloride salt systems across the H_2O-rich to the CO_2-rich regions, *Chem. Geol.*, 2012, **322**, 151-171.

89. M. E. Galvez, C. E. Manning, J. A. D. Connolly and D. Rumble, The solubility of rocks in metamorphic fluids: A model for rock-dominated conditions to upper mantle pressure and temperature, *Earth. Planet. Sci. Lett.*, 2015, **430**, 486-498.

90. C. J. Thompson, J. S. Loring, K. M. Rosso and Z. Wang, Comparative reactivity study of forsterite and antigorite in wet supercritical CO_2 by in situ infrared spectroscopy, *Int. J. Greenhouse Gas Control*, 2013, **18**, 246-255.

91. Q. R. S. Miller, H. T. Schaef, J. P. Kaszuba, G. Gadikota, B. P. McGrail and K. M. Rosso, Quantitative Review of Olivine Carbonation Kinetics: Reactivity Trends, Mechanistic Insights, and Research Frontiers, *Environ. Sci. & Technol. Lett.*, 2019, **6**, 431-442.

92. C. E. Wood, O. Qafoku, J. S. Loring and A. M. Chaka, Role of Fe(II) Content in Olivine Carbonation in Wet Supercritical CO_2, *Environ. Sci. & Technol. Lett.*, 2019, DOI: 10.1021/acs.estlett.9b00496.

93. J. H. Kwak, J. Z. Hu, D. W. Hoyt, J. A. Sears, C. Wang, K. M. Rosso and A. R. Felmy, Metal carbonation of forsterite in supercritical CO_2 and H_2O using solid state ^{29}Si, ^{13}C NMR spectroscopy, *J. Phys. Chem. C*, 2010, **114**, 4126-4134.

94. J. H. Kwak, J. Z. Hu, R. V. F. Turcu, K. M. Rosso, E. S. Ilton, C. Wang, J. A. Sears, M. H. Engelhard, A. R. Felmy and D. W. Hoyt, The role of H_2O in the carbonation of forsterite in supercritical CO_2, *Int. J. Greenhouse Gas Control*, 2011, **5**, 1081-1092.

95. A. Kirfel, T. Lippmann, P. Blaha, K. Schwarz, D. F. Cox, K. M. Rosso and G. V. Gibbs, Electron density distribution and bond critical point properties for forsterite, Mg_2SiO_4, determined with synchrotron single crystal X-ray diffraction data, *Phys. Chem. Miner.*, 2005, **32**, 301-313.

96. T. Pilati, F. Demartin and C. M. Gramaccioli, Lattice-dynamical estimation of atomic displacement parameters in carbonates: Calcite and aragonite $CaCO_3$, dolomite $CaMg(CO_3)_2$ and magnesite $MgCO_3$, *Acta. Cryst. B.*, 1998, **54**, 515-523.

97. G. W. Stephan and C. H. MacGillavry, The crystal structure of nesquehonite, $MgCO_3{\cdot}3H_2O$, *Acta. Cryst. B.*, 1972, **B28**, 1031-1033.

98. M. Jarvinen, Application of symmetrized harmonics expansion to correction of the preferred orientation effect, *J. Appl. Crystallogr.*, 1993, **26**, 525-531.

99. H. J. C. Berendsen, J. R. Grigera and T. P. Straatsma, The missing term in effective pair potentials, *J. Phys. Chem.*, 1987, **91**, 6269-6271.

100. J. G. Harris and K. H. Yung, Carbon dioxide's liquid-vapor coexistence curve and critical properties as predicted by a simple molecular model, *J. Phys. Chem.*, 1995, **99**, 12021-12024.

101. R. T. Cygan, J. J. Liang and A. G. Kalinichev, Molecular models of hydroxide, oxyhydroxide, and clay phases and the development of a general force field, *J. Phys. Chem. B*, 2004, **108**, 1255-1266.

102. W. Smith and T. R. Forester, DL_POLY_2. 0: A general-purpose parallel molecular dynamics simulation package, *J. Mol. Graph.*, 1996, **14**, 136-141.

103. T. B. Fischer, P. J. Heaney, J. H. Jang, D. E. Ross, S. L. Brantley, J. E. Post and M. Tien, Continuous time-resolved X-ray diffraction of the biocatalyzed reduction of Mn oxide, *Am. Mineral.*, 2008, **93**, 1929-1932.

104. Y.-J. Tang, Y.-M. Li, J. Song and Z.-D. Pan, Structural characterization and thermal decomposition behavior of microsized and nanosized $CaCO_3$, *Acta Phys.-Chim. Sin.*, 2007, **23**, 717-722.

105. D. Daval, I. Martinez, J. Corvisier, N. Findling, B. Goffe and F. Guyot, Carbonation of Ca-bearing silicates, the case of wollastonite: Experimental investigations and kinetic modeling, *Chem. Geol.*, 2009, **265**.

106. A. Awad, A. F. K. van Groos and S. Guggenheim, Forsteritic olivine: Effect of crystallographic direction on dissolution kinetics, *Geochim. Cosmochim. Acta*, 2000, **64**, 1765-1772.

107. S. Kerisit, E. J. Bylaska and A. Felmy, Water and carbon dioxide adsorption at olivine surfaces, *Chem. Geol.*, 2013, **359**, 81-89.

108. S. Chen and A. Navrotsky, Calorimetric study of the surface energy of forsterite, *Am. Mineral.*, 2010, **95**, 112-117.

109. H. King, M. Stimpfl, P. Deymier, M. Drake, C. Catlow, A. Putnis and N. de Leeuw, Computer simulations of water interactions with low-coordinated forsterite surface sites: Implications for the origin of water in the inner solar system, *Earth. Planet. Sci. Lett.*, 2010, **300**, 11-18.

110. J. F. Boily, M. Yesilbas, M. M. M. Uddin, B. Q. Lu, Y. Trushkina and G. Salazar-Alvarez, Thin Water Films at Multifaceted Hematite Particle Surfaces, *Langmuir*, 2015, **31**, 13127-13137.

111. J. E. Heath, C. R. Bryan, E. N. Matteo, T. A. Dewers, Y. Wang and C. J. Sallaberry, Adsorption and capillary condensation in porous media as a function of the chemical potential of water in carbon dioxide, *Water Resour. Res.*, 2014, **50**, 2718-2731.

112. C. R. Bryan, T. A. Dewers, J. E. Heath, Y. Wang, E. N. Matteo, S. P. Meserole and D. R. Tallant, *Fundamental study of CO_2-H_2O-mineral interactions for carbon sequestration, with emphasis on the nature of the supercritical fluid-mineral interface*, Sandia National Laboratories, 2013.

113. M. Yeşilbaş and J.-F. Boily, Particle size controls on water adsorption and condensation regimes at mineral surfaces, *Sci. Rep.*, 2016, **6**, 32136.
114. C. A. Grabowski and A. Mukhopadhyay, Comparing the activation energy of diffusion in bulk and ultrathin fluid films, *J. Chem. Phys.*, 2007, **127**.
115. P. F. Low, Influence of absorbed water on exchangeable ion movement, *Clays and Clay Minerals: Proceedings of the Ninth National Conference on Clays and Clay Minerals*, 1960, **11**, 219-228.
116. S. Kerisit and C. Liu, Diffusion and Adsorption of Uranyl Carbonate Species in Nanosized Mineral Fractures, *Environ. Sci. Technol.*, 2012, **46**, 1632-1640.
117. S. Savoye, C. Beaucaire, A. Fayette, M. Herbette and D. Coelho, Mobility of cesium through the callovo-oxfordian claystones under partially saturated conditions, *Environ. Sci. Technol.*, 2012, **46**, 2633-2641.
118. S. Savoye, N. Macé, S. Lefèvre, G. Spir and J. Robinet, Mobility of chloride through cement-based materials under partially saturated conditions, *Appl. Geochem.*, 2018, **96**, 78-86.
119. G. D. Saldi, J. Schott, O. S. Pokrovsky, Q. Gautier and E. H. Oelkers, An experimental study of magnesite precipitation rates at neutral to alkaline conditions and 100-200 °C as a function of pH, aqueous solution composition and chemical affinity, *Geochim. Cosmochim. Acta*, 2012, **83**, 93-109.
120. G. D. Saldi, G. Jordan, J. Schott and E. H. Oelkers, Magnesite growth rates as a function of temperature and saturation state, *Geochim. Cosmochim. Acta*, 2009, **73**, 5646-5657.
121. F. Di Lorenzo, R. M. Rodriguez-Galan and M. Prieto, Kinetics of the solvent-mediated transformation of hydromagnesite into magnesite at different temperatures, *Min. Mag.*, 2014, **78**, 1363-1372.
122. P. Zhang, H. L. Anderson, J. W. Kelly, J. L. Krumhansl and H. W. Papenguth, *Kinetics and mechanisms of formation of magnesite from hydromagnesite in brine, Technical Report SAN099-19465*, Sandia National Labs., Albuquerque, NM (US); Sandia National Labs., Livermore, CA (US), 2000.
123. Q. Gautier, P. Benezeth and J. Schott, Magnesite growth inhibition by organic ligands: An experimental study at 100, 120 and 146 °C, *Geochim. Cosmochim. Acta*, 2016, **181**, 101-125.
124. T. F. Kazmierczak, M. B. Tomson and G. H. Nancollas, Crystal growth of calcium carbonate. A controlled composition kinetic study, *J. Phys. Chem.*, 1982, **86**, 103-107.
125. R. S. Arvidson and F. T. Mackenzie, The dolomite problem; control of precipitation kinetics by temperature and saturation state, *Am. J. Sci.*, 1999, **299**, 257-288.
126. E. Konigsberger, L. C. Konigsberger and H. Gamsjager, Low-temperature thermodynamic model for the system Na_2CO_3-$MgCO_3$-$CaCO_3$-H_2O, *Geochim. Cosmochim. Acta*, 1999, **63**, 3105-3119.
127. M. Hänchen, V. Prigiobbe, R. Baciocchi and M. Mazzotti, Precipitation in the Mg-carbonate system--effects of temperature and CO_2 pressure, *Chem. Eng. Sci.*, 2008, **63**, 1012-1028.
128. C. L. Christ and P. B. Hostetler, Studies in the system MgO-SiO_2-CO_2-H_2O (II); the activity-product constant of magnesite, *Am. J. Sci.*, 1970, **268**, 439-453.
129. D. Di Tommaso and N. H. de Leeuw, Structure and dynamics of the hydrated magnesium ion and of the solvated magnesium carbonates: Insights from first principles simulations, *PCCP*, 2010, **12**, 894-901.
130. X. Zhang, P. Alvarez-Lloret, G. Chass and D. Di Tommaso, Interatomic potentials of Mg ions in aqueous solutions: structure and dehydration kinetics, *Eur. J. Mineral.*, 2019, **31**, 275-287.
131. F. Lippmann, *Sedimentary Carbonate Minerals*, Springer Berlin Heidelberg, Berlin, Heidelberg, 1973.
132. I. M. Power, P. A. Kenward, G. M. Dipple and M. Raudsepp, Room temperature magnesite precipitation, *Cryst. Growth Des.*, 2017, **17**, 5652-5659.
133. J. A. Roberts, P. A. Kenward, D. A. Fowle, R. H. Goldstein, L. A. González and D. S. Moore, Surface chemistry allows for abiotic precipitation of dolomite at low temperature, *Proc. Natl. Acad. Sci. U.S.A.*, 2013, **110**, 14540-14545.
134. D. Liu, Y. Xu, D. Papineau, N. Yu, Q. Fan, X. Qiu and H. Wang, Experimental evidence for abiotic formation of low-temperature proto-dolomite facilitated by clay minerals, *Geochim. Cosmochim. Acta*, 2019, **247**, 83-95.
135. M. Lindner, G. D. Saldi, S. Carrocci, P. Bénézeth, J. Schott and G. Jordan, On the growth of anhydrous Mg-bearing carbonates–Implications from norsethite growth kinetics, *Geochim. Cosmochim. Acta*, 2018, **238**, 424-437.
136. Q. Li and Y.-S. Jun, Salinity-Induced Reduction of Interfacial Energies and Kinetic Factors during Calcium Carbonate Nucleation on Quartz, *J. Phys. Chem. C*, 2019, **123**, 14319-14326.
137. J. K. Lee, S. Banerjee, H. G. Nam and R. N. Zare, Acceleration of reaction in charged microdroplets, *QRBio*, 2015, **48**, 437-444.
138. M. Galib and G. Hanna, Molecular dynamics simulations predict an accelerated dissociation of H2CO3 at the air-water interface, *PCCP*, 2014, **16**, 25573-25582.
139. L. X. Jin, R. Ravella, B. Ketchum, P. R. Bierman, P. Heaney, T. White and S. L. Brantley, Mineral weathering and elemental transport during hillslope evolution at the Susquehanna/Shale Hills Critical Zone Observatory, *Geochim. Cosmochim. Acta*, 2010, **74**, 3669-3691.
140. A. F. White and S. L. Brantley, The effect of time on the weathering of silicate minerals: Why do weathering rates differ in the laboratory and field?, *Chem. Geol.*, 2003, **202**, 479-506.
141. M. F. Hochella and J. F. Banfield, in *Chemical Weathering Rates of Silicate Minerals*, eds. A. F. White and S. L. Brantley, 1995, vol. 31, pp. 353-406.
142. R. Hellmann, R. Wirth, D. Daval, J. P. Barnes, J. M. Penisson, D. Tisserand, T. Epicier, B. Florin and R. L. Hervig, Unifying natural and laboratory chemical weathering with interfacial dissolution-reprecipitation: A study based on the nanometer-scale chemistry of fluid-silicate interfaces, *Chem. Geol.*, 2012, **294**, 203-216.
143. E. Ruiz-Agudo, C. V. Putnis and A. Putnis, Coupled dissolution and precipitation at mineral-fluid interfaces, *Chem. Geol.*, 2014, **383**, 132-146.
144. E. Ruiz-Agudo, C. V. Putnis, C. Rodriguez-Navarro and A. Putnis, Mechanism of leached layer formation during

chemical weathering of silicate minerals, *Geology*, 2012, **40**, 947-950.

145. R. Hellmann, S. Cotte, E. Cadel, S. Malladi, L. S. Karlsson, S. Lozano-Perez, M. Cabie and A. Seyeux, Nanometre-scale evidence for interfacial dissolution-reprecipitation control of silicate glass corrosion, *Nat. Mat.*, 2015, **14**, 307-311.

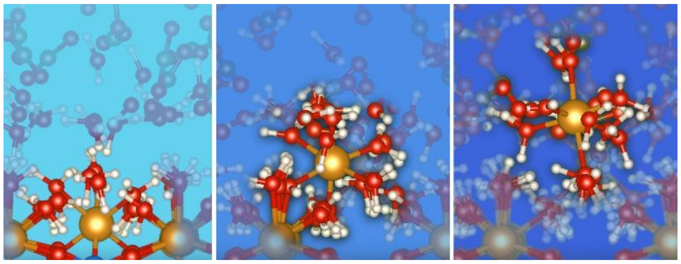

Mineral carbonation reactivity trends and thresholds in nanoconfined water films delineated with in situ X-ray diffraction and molecular simulations.